Shape and Spin State of Asteroid 4179 Toutatis

R. Scott Hudson* and Steven J. Ostro

4 May 1995

R. S. Hudson, School of Electrical Engineering and Computer Science, Washington]] State University, Pullman, WA 99164-2752 USA. S. J. 0s1 ro, Jet Propulsion Laboratory, California Institute of Technology, Pasadena, CA 91109-8099 USA.

Least-squares inversion of an 18-day sequence of delay-Doppler radar images of **Toutatis yields** a **1600-parameter** shape **model and** estimates of **the eight** parameters that, **define the** object's **non-principal-axis** spin state. **Toutatis** is rotating **in** a long-axis mode **characterized by periods** of **5.41** days (rotation about **long** axis) and 7.35 days (average for long-axis **precession). The model's** ratios **of** maximum and **intermediate** to minimum **moments** of inertia **are** 3.19 and 3.01, **and** its **dimensions along the** principal **axes** are **1.92,** 2.40, and 4.60 **km. Although the** asteroid appears cloul~le-lobed **in some** orientations, its **distribution** of **volume** along **the minimum-inertia** axis is not **bimodal. Prominent** topography **includes craters** and ridges. **Either the asteroid's density** is **homogeneous** or its **inhomogeneities mimic the inertia tensor** of **a homogeneous** hoc].y.

Radar measurements of the distribution of echo power in time delay (radial distance) and Doppler frequency (radial velocity) are a unique groundbased source of fine-resolution images of Earth-orbit-crossing asteroids (ECAs). However, a delay-Doppler image is a non-intuitive projection and is subject to global aliasing. Consequently, extraction of all the information contained in such images requires their inversion with a comprehensive physical model. This paper presents results of inverting images that place hundreds of pixels 011 the ECA 4] 79 Toutatis. The resulting model, the most detailed physical characterization of an ECA to date, reveals a geologic.ally complex object in an extraordinary rotation state.

Reconstruction of an asteroid's shape from delay-Doppler images was first achieved for the ECA 4769 Castalia (1) which was resolved into a few doze n pixels per image during a

2.5-h imaging sequence. For Toutatis, observations during 18 consecutive dates in Dec. 1992 (2) placed hundreds to thousands of pixels per image on the target and, quite surprisingly, revealed Toutatis to be in a nonprincipal-axis (NPA) spin state, a situation that dramatically complicates the shape reconstruction process.

For the vast majority of solar system objects the spin vector W is constant and parallel to both the angular momentum vector L and the maximum-moment principal axis of inertia (the object's "short axis"). For such principal-axis (PA) rotation, two constant angles θ and ϕ fix the direction of this rotation pole and another angle $\psi = (2\pi/P)t$, with P the spin period, gives the rotation phase. These three Euler angles give the orientation of the body as a function of time (3).

For a NPA rotator, W is not parallel to L and is not constant in either body-fixed or inertial coordinates. Moreover, all three Euler angles are nonlinear functions of time. The spin vector W is periodic in a body-fixed frame but not in an inertial frame, and in general the object never repeats any given inertial orientation.

For an object with principal moments of inertia $I_s \geq I_i \geq I_l$, where the subscripts refer to short, intermediate, and long axes, the motion is fully determined by specifying at some time t_0 the initial conditions θ_0, ϕ_0, ψ_0, and $\mathbf{W}_0$. Integration of Euler's equations then provides ϕ, θ, ψ, and W as functions of time (3). Since those equations depend on the moments of inertia only through the ratios I_s/I_l and I_i/I_l, a total of eight parameters is needed to fully specify a general spin state. Here we report reconstruction of Toutatis' three-dimensional shape and spin-state based on seventeen Goldstone "low-resolution" (0.5-μs × 0.1 Hz) images from Dec. 2-18 and a single Arecibo (0.2-μs x 0.012 Hz) image from Dec. 19 (4).

Inversion Method. Before iterative, least-squam estimation of the shape and rotation state could begin, a reasonably accurate starting point for scar ching this large parameter space had to be identified. Conveniently, each Toutatis image is bifurcated into a large lobe and a small lobe. We exploited this asymmetry and found that 2.5- km and 1.5-km spheres in contact gave a crude, qualitative representation 01 these images. The Euler angles θ and ϕ then oriented the z axis, through the sphere's centers, with respect to ecliptic coordinates as functions of time, and the Euler angle ψ gave the angular position of the body about this axis.

For each frame, the orientation of this simple shape was estimated "(by hand," with no consideration of the underlying dynamics, by observing the correspondence between observed and modeled data. Due to the shape's symm etry about the z axis, no constraints could be placed on the angle ψ, but this process did produce a series of coarse estimates for O and ϕ in each frame.

We then fit a spin state to these approximate O and ϕ values using the inertia tensor of the two-sphere model in the integration of Euler's equations. W c took the initial time t_0 to be 1992 Dec. 11 at 9:21 UTC, in the middle of the image sequence, when the echoes had the smallest bandwidth and the largest delay depth measured during Dec. 2-19. As discussed by Ostro *et al.*, these two conditions implied that the long axis was close to the radar line of sight (1, OS) and that W -| $\mathbf{W}_{\mathrm{sky}}$, with $\mathbf{W}_{\mathrm{sky}}$ the orbital contribution to the apparent spin vector, also was nearly parallel to the LOS. The resultant, rather crude description of the rotation state provided adequate initial conditions for simultaneous least-squams estimation of the full set of parameters describing the asteroid's shape, radar scattering properties, and

dynamics. Following the approach used for Castalia (1), we minimized an objective function of the form

$$\Phi(\mathbf{s},\mathbf{p},\mathbf{d}) = \chi^2(\mathbf{s},\mathbf{p},\mathbf{d}) + 10^{\beta_A} A(\mathbf{s}) + 10^{\beta_B} B(\mathbf{s},\mathbf{d}) + 10^{\beta_C} C(\mathbf{s}) + 10^{\beta_D} D(\mathbf{d}) \quad (1)$$

where the vectors s, **p**, and **d** denote the shape, "photometric," and dynamical parameters of the model; χ^2 is the least-squares goodness-of-fit measure; and $A(\mathbf{s})$, $B(\mathbf{s},\mathbf{d})$, $C(\mathbf{s})$, and $D(\mathbf{d})$ are penalty functions.

We modeled the differential radar cross section of the surface (5) as

$$\sigma_0 = \rho \cos^n i \quad (2)$$

with i the angle of incidence, ρ the normal reflectance, and n a measure of surface specularity. Eighteen parameters $\rho_k = \rho/\mathrm{SDEV}_k$, with SDEV_k the radar cross section equivalent of one standard deviation of receiver noise, gave independent estimates of ρ for each frame (6). These and n defined 19 photometric parameters **p**.

The dynamical parameters included, $I_s/I_l, I_i/I_l, \phi_0, \theta_0, \psi_0, \mathbf{W}_0$, and six rotational offsets for each frame: $\Delta\phi_k, \Delta\theta_k, \Delta\psi_k$, and $\Delta\mathbf{W}_k$, $1 \le k \le 18$. The offsets were added to the calculated Euler angles and spin vector in the initial stages of the estimation. Weakly weighting $D(\mathbf{r})$, the sum of the squares of the rotational offsets, enabled a random spin state from frame to frame, while a strong weighting forced the offsets toward zero and hence

enforced consistency with Euler's equations, a physical requirement of the final model. We gradually increased β_D until the dynamical offsets were on the order of 1° or 1°/day, at which point we set all offsets to zero. Additional dynamical parameters, $\Delta\tau_k, \Delta\nu_k, 1 \leq k \leq 18$, allowed for correction of the observing ephemerides' predictions [2] of the delay-Doppler locations of the center of mass (COM) in each frame.

A(s) penalized deviation of the centroid of the shape from the dynamical COM. B(s, cl) penalized deviation of the inertia tensor of the shape, computed assuming uniform density (UD), from the inertia tensor used to describe the spin state. Setting β_A and β_B very large enforced consistency of the model with UD. This was not an *a priori* requirement, but these penalty functions let us test the UD hypothesis. If enforcing consistency with UD significantly raised χ^2, the hypothesis would be rejected; otherwise it would remain viable.

The function C(s) penalized surface concavities; setting β_C large forced the shape toward convexity and ensured that only those features that are absolutely needed to explain the observed data were allowed. Indeed we took β_C large enough that it visibly smoothed out the modeled delay-Doppler images and suppressed some apparently real topography near the scale of the data's resolution (7).

Delay-Doppler radar images typically have a large dynamic range, and the imaging geometry usually results in much brighter pixels near the leading edge of the object. To more equitably weight all regions of the object in the fits, we applied a gamma correction (8) with $\gamma = 2$ to observed and modeled data throughout the estimation process.

In the initial fits we floated the diameters and locations of the two (potentially overlapping) spheres along with the dynamical and photometric parameters. The shape was

simplistic and not expected to correspond to the asteroid's inertia tensor, so we left it decoupled from the dynamical parameters. This process resulted in an improved solution for **d**. Then each sphere was replaced with a spherical harmonic series model as in the reconstruction of Castalia (1). At first, low-resolution shape models were used and the penalty functions were weakly weighted. When the spin state and shape had evolved sufficiently that features on the order of the spatial resolution of the shape model were being fit throughout the 18-day sequence, we moved to progressively longer series.

There are enough pixels in the data used here to constrain more than a thousand shape parameters, but spherical harmonic models become computationally burdensome with more than a few hundred coefficients. After solving for a few hundred parameters, we moved to polyhedral models defined by a set of vertices $\mathbf{v}_i$, $1 \leq i \leq N$, grouped into triples to define triangular surface facets (9). Exact closed-form expressions exist for the centroid and inertia tensor of such models, they are more efficient to render with large numbers of shape parameters, and they can describe an arbitrary closed shape.

We parameterized the shape as a deformed ellipsoid via

$$\mathbf{v}_i = \mathbf{a}_i + r_i \mathbf{u}_i \qquad (3)$$

where the $\mathbf{a}_i$ were points on an ellipsoid (the inertia ellipsoid of the previous best-fit model) and the $\mathbf{u}_i$ were the surface normals of that ellipsoid. The free shape parameters r_i specified the deviation of the shape from this ellipsoid. Replacing the $\mathbf{u}_i$ with the surface normals of the converged model led to no significant change in the reconstruction, supporting our impression that this parameterization was sufficiently general. We began with N = 200

vertices and increased N to *400*, *800*, and finally 1600, at each stage allowing the fit to converge. Additional vertices were added by repeatedly halving the shape's longest facet edge; this process resulted in a fairly uniform distribution of vertices over the surface. The final $N = 1600$ model (10) has 3196 facets whose average area is $(84 \text{ m})^2$.

Shape. Figure 1 shows renderings of the Toutatis model from six different view points and with two different illumination geometries. In (A) zero-phase illumination (source and observer co-located) shows the overall shape and dimensions, and in (B) the source is moved 75° toward the top of the page to let shadowing effects bring out details of surface features. The model has a volume of *7.67* km^3 and a surface area of 22.5 km^2, which is 19% larger than the surface area of a sphere of the same volume. The volume defines an effective diameter 2.45 km (11).

A simple, but useful, approximation to Toutatis's figure is an ellipsoid for which I_s/I_l, I_i/I_l, and the volume are the same as for Toutatis. This ellipsoid has overall dimensions *(1.70,2.03,4.26)* ± *0.08* km. The "dynamical elongation" of Toutatis is 4.26/1.70 = 2.51 ± 0.15. The ratios of the maximum extent of the actual shape in the long-axis direction to the maximum extents in the short- and intermediate-axis directions, *4.60/1.92 = 2.40:1* 0.13 and 4.60/2.28 = 2.02 ± 0.10, describe the asteroid's "physical elongation."

Toutatis radar images appear bifurcated in every frame (2), and a natural inference is that the object is itself bifurcated in some sense. The intermediate- and short-axis views of Fig. 1 (A) lead us to perceive the shape as consisting of two lobes, which we label 1,1 and 1,2. Lobe 1,1 accounts for about 2/3 of the long axis dimension, 1,2 for about 1/3. However, with UD assumed, the asteroid's mass distribution along the long axis is not bimodal (Fig.

2).

The most prominent features at the several-} IIIrIc; lc{l-lIl(:tcl scale include the concavities labeled Cl, C2 and C3 in Fig. 1 (B). Cl and C2 are the most circular, and we identify these as impact craters. Their c1osc proximity and similar diameters (about *750* m) arc intriguing. C3, which extends over most of the length of L2, is less circular but also may be an impact structure.

The pattern of ridges R1, R2, and R3 dominate the relief in some views. The largest of these, R1, extends about 1 km across L1 and is oriented nearly normal to the asteroid's long axis. This is followed by a shorter ridge, R2, closer to L2. Feature R3 appears, in some views, to be an extension of the structure R1-R2.

The 500-m-deep "neck" N extends part way around the the opposite side of the asteroid from the structure R1-R2-R3, demarcating 1,1 and 1,2 in many views, The corresponding appearance of these features in the observed and modeled delay-l)o~)plm images is shown in Fig. *3* for five frames.

The model's scattering law is nearly Lambertian (n = 2.3:1 0.5). This result and the echoes' polarization signature (2) imply that Toutatis's surface is very rough at Cln-to-in scales.

Spin State. Toutatis' extraordinary rotation is specified by the following initial conditions. The moment ratios are within 3% of I_s/I_l = 3. I 9 and I_i/I_l = 3.01. At t_0, the Euler angle.s of the principal axes of inertia with respect to ecliptic coordinates were within 3° of ϕ_0 = - 103°, θ_0 = 94°, ψ_0 = ' 136°, while the projection of $\mathbf{W}_0$ along the (short, intermediate, lo ıg) principal axes was within 1° day^{-1} of (20°, 32°,980) day^{-1}.

These eight parameters define the direction of 1, as ecliptic longitude - 3°, latitude - 53°. The fact that $L^2/2EI_1 = 0.55$, with E the rotational kinetic energy, is less than unity identifies the spin state (3) as a "long axis mode.' W, in lmly-fixed coordinates, rotates about the long axis every $P_1 = 5.41$ days, and during this time the angle between the long axis and **L** varies twice between 49° and 500 The complete motion consists of nonlinear periodic variations every P_1 superposed on a uniform rotation about **L** every $P_2 = 7.35$ days.

Figure 4 shows the reconstructed shape and spin state of Toutatis in an inertial frame at six-hour time intervals beginning 3 Dec. 1992 at 18:00 UTC; the entire sequence spans 7.25 days. The view is from above the plane of the ecliptic and illumination is provided by an artificial source 45° counter- clockwise! from the top of the page and 30° out of the page toward the viewer. The long axis moves from being nearly in the plane of the ecliptic to nearly perpendicular to it, and the long-axis orientation (O, ϕ) almost repeats after the 7.25 days. However, the orientation of the body about the long axis (ψ) is quite different between the beginning and end of this sequence, demonstrating how the complete motion of the object is not periodic (12).

Note the similarity between the Dec. 2 and Dec. 13 delay-lh~l~)lcl images in Fig. 3. This means that on each date: 1) the orientation of W with respect to the asteroid was nearly the same, and 2) nearly the same region of the surface was visible. Condition 1 occurred because the $\sim$ 1 0.5-day interval between these images is nearly $2P_1$; a combination of the object's rotation and more than 1000 of plane-of-sky (POS) motion produced condition 2.

The delay-Doppler projection is invariant with respect to a rotation of the object/sl)iI~ state about the radar], OS. However, 1'OS motion can break this ambiguity, and for Toutatis

the POS motion was more than 100° during the 18 days of radar observations. Here the least squares solution is sensitive to all spin state parameters, and rotating the initial conditions about the LOS at t_0 produces a poor fit. Nonetheless, it is desirable to have independent, post-modeling, confirmation of the model's prediction of the POS orientation.

On 17 Dec. at about 7:25 UTC, the Very Large Array (VLA) achieved POS resolution of Toutatis echoes of a Goldstone transmission (1 3). Although the resolution of 0.2 arcsec, equivalent to 10 km at the asteroid, did not resolve the object, an elongation at a position angle of about - 61° was revealed in the difference between the image and a point source model. Figure 5(A) shows our model's prediction for Toutatis's orientation during the time of this observation; the line running through the model is the Goldstone-VLA prediction. This observation was fortunate to catch Toutatis at a time when its long axis was nearly parallel to the plane of the sky.

The Hubble Space Telescope (HST) imaged Toutatis on 10 1 Dec. about 18:40 UT when the Sun-Toutatis-Earth angle was about 90". Image pixels subtended 926 m on the asteroid (0.0439 arcsec), and the FWHM of the core of the point spread function was 0.070 arcsec, corresponding to a resolution of 1.48 km at Toutatis. Fig. 5 (B) shows our predicted appearance of Toutatis; Fig. 5 (C) shows the same view with a pixel size of 453 m for comparison with Fig. 4 of Nell *et al.* (14). The rendered model, with a maximum dimension of *2.2* km, is consistent with those authors' statement that the illuminated, visible area was "most likely in the range from 1.7 to 2.4 km." Noll *et al.* also interpreted the HST data as suggesting an "extended feature at an angle of about 45° off the solar vector, " which is indicated by the line through Fig 5 (C). Fig. 5 (B) shows that this apparent elongation was

due to the unusual shape of Toutatis and shadowing effects arising from the large illumination angle.

After having estimated both the shape and the spin state of Toutatis, it was apparent that the entire surface of Toutatis was observed by the 18 radar images. Therefore, no area of our model is unconstrained. Moreover, since Toutatis is a NPA rotator, the entire inertia tensor (to within a constant factor) is observable. Because of these two facts we would expect that, as discussed above, enforcing a UD hypothesis through penalty functions would provide a powerful test of homogeneity. We investigated this possibility at several stages by removing the dynamical penalties which couple the inertia tensor and the shape. No significant change occurred in the fit. That is, evidence for a nonuniform distribution of density is lacking. Apparently either Toutatis is nearly homogeneous, or its inhomogeneities mimic the inertia tensor of a homogeneous body.

Discussion. The shapes and spin states of asteroids are believed to be primarily the products of violent collisional histories. For the great majority of asteroids it is thought that damping of NPA to PA rotation occurs at time scales much shorter than the mean time between collisions. Therefore, whereas violent collisions would be expected to produce NPA rotation, it is not surprising that lightcurves for several hundred asteroids overwhelmingly indicate PA rotation. Due to its very slow rotation, the damping time scale for Toutatis is believed to be orders of magnitude greater than the age of the solar system (1 5), so Toutatis provides a remarkably well-preserved relic of a collision-induced spin state.

The source of Toutatis' topographic bifurcation is a mystery. Unlike Castalia, Toutatis's shape does not evoke a "contact-binary" configuration. On the other hand, it seems unlikely

(but certainly not impossible) that feature N could have been sculpted by a direct impact. Similarly, it is not clear what sequence of impacts might be responsible for the 1{1-1{2-1{3 structure. Other pertinent questions involve the implications of surface topography for the asteroid's internal configuration, e.g., for it's cohesiveness (16). Collisional simulations using the Toutatis model may resolve these issues.

Fully desmeared, high-resolution images from the 1992 radar experiment should support modeling with an order of magnitude more shape parameters than used here, and the resulting fine morphological detail available should shed even more light on Toutatis' geology. Given recent spacecraft and radar results, it is quite clear that the shapes and spin states of asteroids are strange and variegated, presumably the outcomes of collisional processes that remain poorly understood (17). As the collection of detailed shape models continues to grow, we can expect commensurate improvement in our understanding of the physics of these fascinating small worlds.

REFERENCES AN I)NOTES

1. R. S. Hudson and S. J. Ostro, *Science* 263, 940 (1994).

2. S. J. Ostro *et al.*, submitted for publication.

3. L. D. Landau and E. M. Lifshitz, *Mechanics* (Pergamon Press, New York, 1976), chap 6; N. 11. Samarasinha and M. II'. A'Hearn. *Icarus* 93, 194 (1991); M. J. S. Belton, W. 11. Julian, A. J. Anderson, B. E. A. Mueller. *Icarus* 93, 183 (1991).

4. For Goldstone the transmitter frequency and wavelength were F_{TX} = 8510 MHz, λ = 3.52 cm; for Arecibo they were F_{TX} = 2380 MHz, λ = 12.6 cm. The radial velocity equivalent of 1 Hz is $(\lambda/2)$ sec^{-1}.

5. The radar cross section of a surface element of area dS is $\sigma = \sigma_0\, dS$.

6. The ρ_k express the reflectance in units of standard deviations of receiver noise. Calibration of the SDEV$_k$ at a future date may allow p to be expressed in absolute units.

7. Our rationale for being very conservative with β_C is the existence of higher-resolution images that place several times as many pixels 011 Toutatis as those used in the present modeling process. Those data will provide the most effective constraints on the sub-hundred-meter scale structure of the surface. Yet, the proper desmearing of those images required the COM locations from the solution reported here. In that sense, the model described in this paper is an initial condition for subsequent, higher-resolution modeling.

8. This is equivalent to replacing each pixel value by its square root.

9. 1). Hearn and M. P. Baker, *Computer Graphics* (Prentice Hall, Englewood Cliffs, NJ, ed. 2, 1994), chap. 10.

10. Increasing N beyond 1600 did not appreciably improve the fits.

11. Thermal modeling by various researchers had suggested effective diameters between 2.0 and 3.0 km. D. J. Tholen, *Bull. Amer. Astr. Soc.* 24, 934 (1992); D. II'. Lupishko, S. V. Vasilyev, Ju. S. Efimov, N. M. Shakhovskoj, *Icarus* **113**, 200 (1995).

12. J, R. Spencer *et al., Icarus* (in press), attempted to deduce the spin period of Toutatis from optical lightcurves under the assumption of I'A rotation. They found a best fit for P = 7.25 days, but concluded from the poor fit that the rotation was probably complicated. From Fig. 4 it appears that their analysis identified the quasi-periodic orientation of the long axis. Failure of the lightcurves to display truly periodic behavior is due to the incommensurability of ϕ, 0, and ψ.

13. 1. de Pater *et al.*, *Icarus* **111**, 489 *(1994)*. See Fig. 12b.

14. K. S. *Nell,* 11. A. Weaver, A, D. Storrs, B. Zellner, *Icarus* **113**, *353 (1995).*

15. A. W. Harris. *Icarus* **107**, *209 (1994);* J. A. Burns and V. S. Safronov, Mon. *Not. R. Astron. Soc. 165,* 403 (1 973).

1 (i. W. F. Bottke, Jr., and J. J, Melosh, *Lunar Planet Sci. Conf. Abstr. 26,* 153 (1 995).

17. 1{. R. Housen and K. A. Holsapple, *Icarus* 84, 226 (1990).

18. Part of this research was conducted at the Jet Propulsion laboratory, California Institute of Technology, under contract with the National Aeronautics and Space Ad-

ministration (NASA). Work at Washington State University was supported in part by NASA.

FIGURE LEGENDS

1. (A) Renderings of the Toutatis model from both directions on the long, snort, and intermediates axes (left, center, right columns). The bar at the upper left is 1 km long. Labels denote surface features discussed in the text. Source and observer are co-located. (B) Same as (A) but the source of illumination is moved 75° towards the top of the page. Lambertian scattering is used in all renderings.

2. Cross sectional area vs. position on long axis for Toutatis model and the lower-bound Castalia model (1). For comparison, both models were normalized to unit volume and unit long axis length. Given uniform density, the curves would also correspond to mass distribution.

3. Observed and modeled delay-Doppler images for five dates. Residuals (difference of observed and modeled data) have been scaled up to use all the available dynamic range. Labels correspond to features in Fig. 1.

4. Toutatis shape and spin state rendered at six hour intervals beginning 3 Dec. 1992, 18:00 UTC and increasing left to right, top to bottom. Each row spans two days; the total sequence covers "i" .25 days. The bar at the lower left is 1 km long. The view is looking south along the ecliptic pole with the vernal equinox to the right. An artificial source is located 45° counter clockwise from the top and 30° out of the page.

5. (A) Toutatis model at 17 Dec. *1992, 7:25* UTC with zero-Doppler illumination. North is up. The line passes through the COM and is the Goldstone-VLA prediction (Fig. 3) of Toutatis's elongation at that time. (B) Toutatis model at 10 Dec. 1992, 18:40 with

correct solar illumination. North is 112.8° clockwise from up. (C) Same as (B) but with 453-m pixels. The line passes through the COM and corresponds to the apparent elongation of Toutatis in HST images (14).

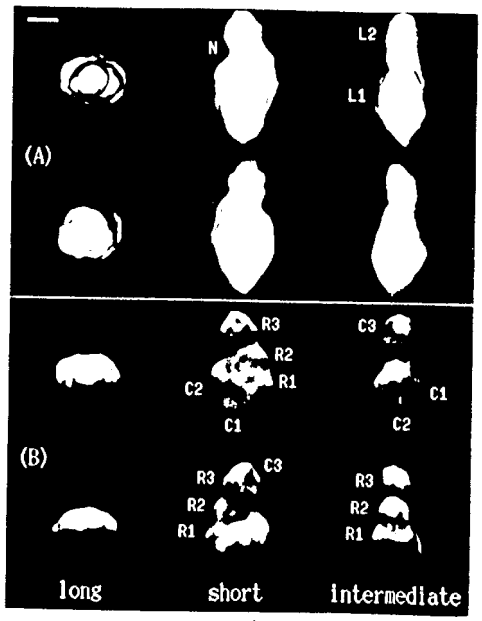

FIG. 1

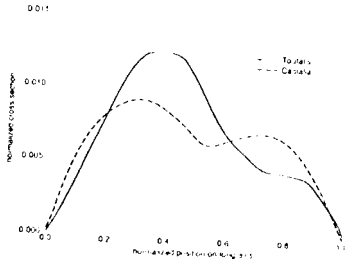

FIG. 2

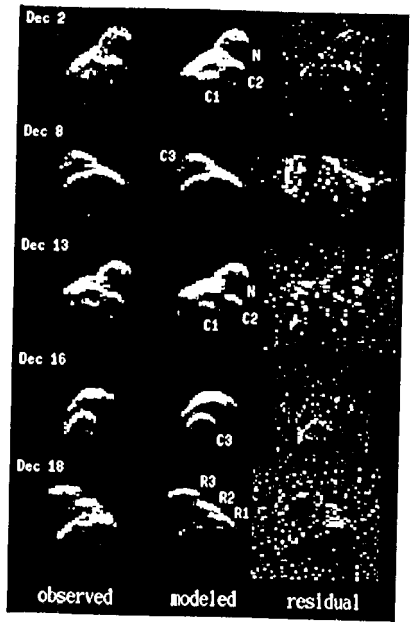

FIG. 3

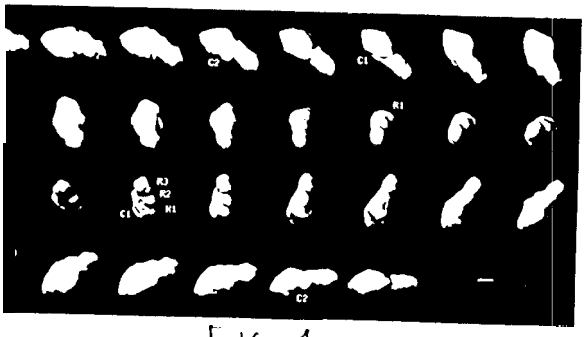

FIG. 4

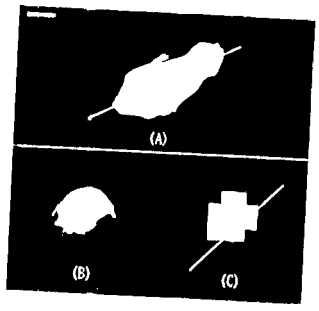

FIG. 5